Construction and Building Materials 443 (2024) 137690

Contents lists available at ScienceDirect

Construction and Building Materials

journal homepage: www.elsevier.com/locate/conbuildmat

Self-prestressing bonded patches using Fe-SMA and CFRP for lifetime extension of fatigue-cracked steel details

Sizhe Wang [a,b,c,*], Qingtian Su [b], Xu Jiang [b,**], Lingzhen Li [a,d,e], Masoud Motavalli [a], Elyas Ghafoori [a,b,d,f]

[a] Empa, Swiss Federal Laboratories for Materials Science and Technology, Structural Engineering Research Laboratory, Überlandstrasse 129, Dübendorf 8600, Switzerland
[b] College of Civil Engineering, Tongji University, Shanghai 200092, China
[c] Singapore Centre for 3D Printing, Nanyang Technological University, Singapore
[d] Institute of Structural Engineering (IBK), Department of Civil, Environmental and Geomatic Engineering, ETH-Zürich, Zürich 8093, Switzerland
[e] Department of Civil and Environmental Engineering, The Hong Kong Polytechnic University, Hong Kong, China
[f] Institute for Steel Construction, Faculty of Civil Engineering and Geodetic Science, Leibniz University Hannover, Hannover 30167, Germany

ARTICLE INFO

Keywords:
Iron-based shape memory alloy (Fe-SMA)
Memory-steel
Carbon fiber reinforced polymer (CFRP)
Adhesive bonding
Metallic structure
Fatigue
Repair

ABSTRACT

Self-prestressing bonded patches employing iron-based shape memory alloy (Fe-SMA) and carbon fiber reinforced polymer (CFRP) for lifetime extension of cracked steel structures are investigated. The repair patches, applicable in confined spaces, are bonded over cracks, with prestress generated within Fe-SMA via activation (heating and cooling) to induce compression on cracks. Experimental tests involve cracked steel plates repaired with Fe-SMA and Fe-SMA/CFRP bonded patches, with a patch width of 50 mm and varied patch lengths of 100—500 mm. Fe-SMA strips are activated to 180 ℃ using electric heating, generating prestresses of 154—254 MPa. Fatigue tests ($\Delta\sigma$=90 MPa, R=0.2) show fatigue life extensions of $\geq$ 4.2 and $\geq$ 5.5 times for Fe-SMA and Fe-SMA/CFRP repairs. The 100 mm long Fe-SMA/CFRP patch exhibits optimal performance in lifetime extension, achieving complete crack arrest. As patch lengths decrease, failure modes shift from Fe-SMA (and CFRP) fracture to patch debonding while all patches remain effective in fatigue life extension. Finite element analysis with experimental validation quantifies the effects of prestress and load-sharing on reducing stress intensity factors at crack tips, thus retarding crack propagation. Design recommendations are proposed for the application of self-prestressing patches.

1. Introduction

Fatigue is one of the major challenges to the long-term service of steel structures across various industrial sectors, such as bridges, wind turbines, gantry cranes, automotive, and maritime facilities. Timely intervention for fatigue cracks is essential in preserving integrity and functionality of steel structures, prolonging their service lifetime, while minimizing potential economic and environmental impacts due to structural failures [1]. Proper design, manufacturing, and maintenance practices are important to prevent fatigue crack initiation. Meanwhile, it is significant to implement effective repair solutions to inhibit fatigue crack propagation once cracks manifest.

1.1. Fatigue repair techniques

Many techniques were developed to retard fatigue cracks, such as welding repair, welding cover plates, single peak tensile overloads, crack-arrest holes, and adhesively bonded carbon fiber reinforced polymers (CFRP) [2]. Among these techniques, cold-worked crack-arrest holes filled with steel pins and bonding CFRP patches showed superior retardation performance [2]. In the past decades, the technique of bonded CFRP patches has attracted much research attention owing to its

* Corresponding author at: Empa, Swiss Federal Laboratories for Materials Science and Technology, Structural Engineering Research Laboratory, Überlandstrasse 129, Dübendorf 8600, Switzerland.
** Corresponding author.
E-mail addresses: sizhe.wang@ntu.edu.sg (S. Wang), sqt@tongji.edu.cn (Q. Su), jiangxu@tongji.edu.cn (X. Jiang), lingzhen.li@polyu.edu.hk (L. Li), masoud.motavalli@empa.ch (M. Motavalli), ghafoori@stahl.uni-hannover.de (E. Ghafoori).

https://doi.org/10.1016/j.conbuildmat.2024.137690
Received 5 February 2024; Received in revised form 26 July 2024; Accepted 29 July 2024
Available online 3 August 2024

advantages such as non-destructive repair, light weight, convenient implementation, applicability on curved surfaces, and excellent static, fatigue, and corrosion performances [2,3]. Repair of fatigue cracks using non-prestressed bonded CFRP patches was studied across various scenarios, including single-side or double-side repairs, mode I or mixed mode I/II cracks, and different damage levels [4–10].

The bond performance and environmental durability were critical issues for the bonded CFRP repair technique [11]. To this end, various studies were conducted to understand the static and fatigue behaviors of the CFRP-to-steel bonded joints [12–15]. The effects of environmental factors such as temperature, moisture, seawater, and ultraviolet radiation were investigated [16–19]. Proper surface treatment demonstrated effectiveness for enhancing bond durability, and consideration of environmental and long-term partial factors in the design process was necessary to ensure the bond performance [18]. In addition, direct contact between carbon fiber and steel posed a risk of galvanic corrosion, whereas the application of an epoxy layer proved effective in preventing this corrosion [20–22].

Furthermore, repair solutions using prestressed un-bonded/bonded CFRP showed promising in fatigue crack repair, enabling crack arrest through prestress application [23–29]. However, the prestressing process of CFRP usually requires hydraulic jacks and reaction facilities, while its anchorage often needs mechanical clamps. These are generally too cumbersome for local crack repair, sometimes even impossible owing to limited space, hindering its practical application [23–29]. In addition, mechanical anchorages involving drilling holes are usually undesirable for fatigue-sensitive structures, while non-destructive bonding technique is preferable.

More recently, shape memory alloys (SMAs) were exploited for prestressed strengthening. The shape memory effect of SMA enables prestressing through an activation process (commonly a controlled heating operation followed by cooling), which is significantly easier compared to mechanical tensioning, particularly in confined spaces. A patching system consisting of nickel-titanium-based shape memory alloy (NiTi-SMA) wires and CFRP sheets was developed, and experimental tests indicated its effectiveness for fatigue crack repair [30–35]. Cracked steel plates repaired with the NiTi-SMA/CFRP composite patches, with only CFRP sheets, and with only NiTi-SMA wires exhibited fatigue lives that were 26.4, 8.0, and 1.7 times those of the unrepaired specimens, respectively [31].

In addition to NiTi-SMAs, iron-based shape memory alloys (Fe-SMAs) [36,37] were utilized for fatigue crack repair. Izadi et al. [38,39] employed Fe-SMA strips that were anchored through bolted clamps to repair cracked steel plates and angle connections. Wang et al. [40,41] studied bonded Fe-SMA strips on cracked steel plates. Crack repairs using bonded non-prestressed CFRP plates, bonded non-prestressed Fe-SMA strips, and bonded prestressed Fe-SMA strips were compared, showing that the fatigue lives were extended by 1.70, 2.61, and 3.51 times, respectively [40]. Different heating methods to activate the bonded Fe-SMA strips were investigated, such as using a heat gun, hot bonder, and gas torch [41]. Moreover, complete fatigue crack arrest could be achieved by adjusting the Fe-SMA strip dimensions and activation temperature [41,42]. Qiang et al. [43,44] repaired cracks at the diaphragms in orthotropic steel bridge decks by combining crack-arrest holes and bonded Fe-SMA strips, and long-term monitoring showed no subsequent crack propagation after repair.

1.2. Motivation and significance of the current study

Previous studies have demonstrated the effectiveness of self-prestressing bonded patches employing SMAs for fatigue crack repair. Compared to NiTi-SMA, Fe-SMA is more cost-effective, more efficient in prestressing, and easier to implement. This study further explores the repair technique of self-prestressing bonded patches using Fe-SMA and delves into the following primary problems.

(1) Evaluation of prestress. Fig. 1a illustrates the key mechanism for self-prestressing repair patches employing Fe-SMA [40]. The shape memory effect of the Fe-SMA is activated through a heating and cooling process; as the recovery strain of the bonded Fe-SMA is restrained, it generates a prestress, inducing compression on cracks. The final prestress within the patch is a critical variable. Unlike mechanical tensioning, the prestress of a bonded Fe-SMA strip cannot be directly measured, necessitating extensive research to establish a reliable prestress estimation approach. Therefore, one of the emphasis of this study is to carefully control and monitor the activation process to evaluate the final prestress and to quantitatively examine the prestress effect on crack retardation.

(2) Optimal Patch length. A common question in designing the repair patch is to determine the appropriate patch length. A compact patch is desirable for material conservation and applicability in confined spaces (e.g., in orthotropic steel bridge decks, wind turbines, etc.). While sectional dimensions can be designed based on crack conditions, geometry, and desired sectional stiffness and prestress forces [25], the patch length is critical for the success of the patches from the following aspects: (a) The bond capacity depends on the bonded length [45]; (b) The Fe-SMA prestress level is influenced by the activation and anchorage lengths [46]; (c) The stress distribution in the parent structure caused by Fe-SMA prestress relates to the activation length [40]. Therefore, the patch length is a vital parameter for repair effect, bond capacity, and material efficiency.

(3) Combination of Fe-SMA and CFRP. A bonded patch combining Fe-SMA strips and CFRP sheets provides an alternative that balances the advantages of both materials: Activated Fe-SMA strips can provide prestresses and share loads, while CFRP sheets, with the advantages of flexibility, light weight, and cost-effectiveness, can accommodate curved geometries, offer additional stiffness, ensure smooth stress transfer, and protect the bonded Fe-SMA strips from environmental invasions. Fig. 1b shows a potential application example of using both Fe-SMA and CFRP for repair. Therefore, two types of self-prestressing bonded patches, employing Fe-SMA and Fe-SMA/CFRP, are investigated.

In this study, seven cracked steel plates are tested, one as a reference, two repaired with bonded Fe-SMA strips, and four repaired with Fe-SMA/CFRP patches. The Fe-SMA strip lengths of these repair patches vary in a range of 100–500 mm. The specimens undergo an Fe-SMA activation process using well-controlled electric heating with meticulous monitoring, and the Fe-SMA prestress is assessed based on experimental measured strains and numerical simulations. The fatigue repair effectiveness is evaluated through the experimental fatigue life extensions, and crack behavior is analyzed through stress intensity factors (SIFs) at the crack tips. Ultimately, design recommendations are proposed.

This study primarily focuses on the repair effectiveness of the patches in addressing fatigue issues, while the durability of the repair patches, though being an important aspect, remains beyond the scope of the current study.

2. Materials

2.1. Fe-SMA

The Fe-SMA strips used in the study were “memory-steel” from re-fer AG, Switzerland, with a composition of Fe–17Mn–5Si–10Cr–4Ni–1(V, C). The Fe-SMA strips were 2 % prestrained in the factory and delivered in 1.5 mm thick strips. Extensive research has examined various properties of the Fe-SMA, such as transformation temperatures and recovery stresses [37,47–49], static and fatigue behavior [50–52], and corrosion and temperature resistances [37,53,54]. The main mechanical

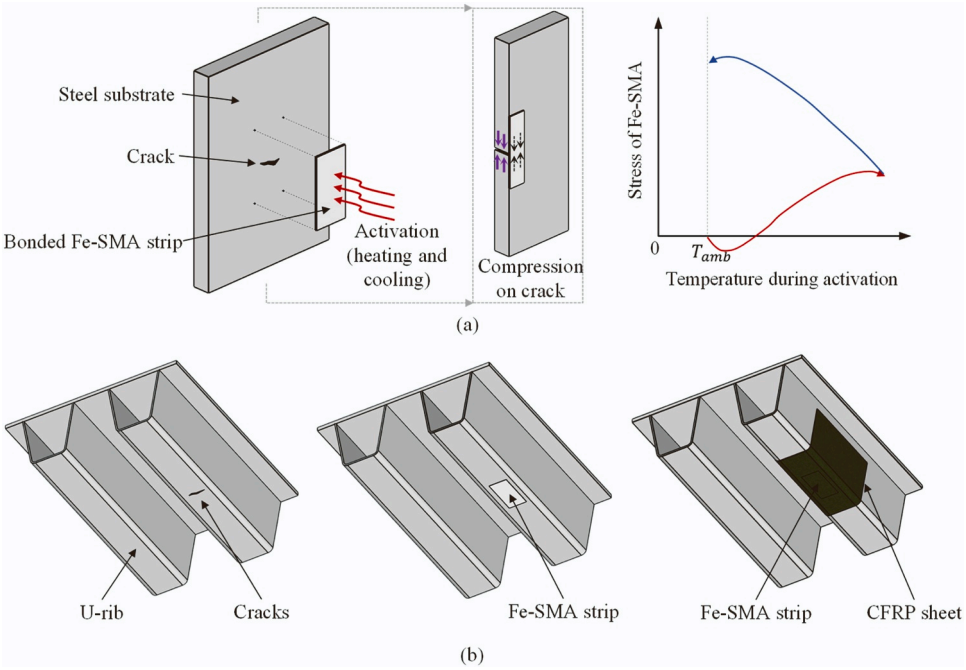

Fig. 1. Repair of fatigue-cracked steel structural details using self-prestressing bonded patches. (a) Key mechanism: activate Fe-SMA through heating and cooling to gain prestress, inducing compression on crack. (b) An application example in orthotropic steel bridge decks. Fe-SMA: iron-based shape memory alloy; CFRP: carbon fiber reinforced polymer; T_{amb}: ambient temperature.

properties of the Fe-SMA are summarized in Table 1 and its recovery stresses (σ_{rec}) by different activation temperatures (T_{act}) are shown in Fig. 2. For more detailed characterizations of the Fe-SMA, readers can refer to [47,48,50–53].

2.2. Carbon fiber sheet

CFRP consisted of carbon fiber sheets and epoxy resin adhesives. The carbon fiber sheets used were S&P C-sheet 240 (200 g/m^2) [57], which are unidirectional carbon fiber fabrics with a design thickness of 0.113 mm. Table 1 shows the main mechanical properties of the carbon fiber sheets.

2.3. Adhesives

2.3.1. SikaPower-1277 for bonding Fe-SMA

A two-component epoxy adhesive SikaPower-1277 (with a pink color) [58–60] was employed for bonding Fe-SMA strips to steel plates.

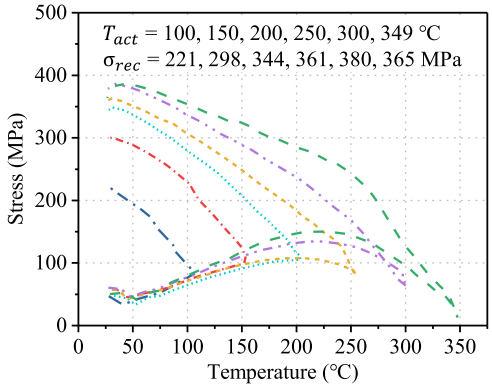

Fig. 2. Recovery stresses of Fe-SMA by different activation temperatures [48].

Table 1
Materials properties.

	Fe-SMA strips (memory-steel) [55, 56]	Carbon fiber sheet (S&P C-sheet 240) [57]	Adhesive (SikaPower-1277) [58–60]	Adhesive (S&P Resin 55 HP) [61]	Steel plates [25]
Elastic modulus (GPa)	164	240	2	≥3.2	205
Yield strength (MPa)	424[a]	-	-	-	421
Ultimate strength (MPa)	1042	4400	30	≥100[b]	526
Lap-shear strength (MPa)	-	-	28[c]	≥50	-
Ultimate elongation (%)	53	1.8	4	-	-
Glass transition temperature T_g (℃)	-	-	67	53	-
Thickness (mm)	1.5	0.113	≥0.3	-	10

[a] It refers to the 0.2 % yield stress $\sigma_{y0.2}$.
[b] It refers to compressive strength (for the other materials, the ultimate strength refers to tensile strength).
[c] It is provided by the manufacturer, obtained through lap-shear tests of steel bonded joint with dimensions of 25 × 10 mm [58]. Usually, bond capacity increases with bond length up to the effective bond length and then reaches a plateau, while average shear strength decreases with bond length because of non-uniform stress distribution. Lap-shear tests of Fe-SMA-to-steel bonded joints indicated an effective bond length of approximately 120 mm with an average shear strength of 10 MPa [55,62].

Table 1 shows the main thermomechanical properties of the adhesive. The adhesive has a glass transition temperature (T_g) of approximately 67 °C [58,59]. Additionally, the adhesive exhibits a temperature resistance up to 180 ℃ (its shear strength declines after exposure to temperatures above 180 ℃) [55,60], while a study indicated that an activation of bonded Fe-SMA strips to 180 ℃ slightly increased the bond capacity of the adhesive [63]. Therefore, a target activation temperature of 180 ℃ was selected for the Fe-SMA activation in this study, as detailed in Section 3.2.3.

2.3.2. S&P Resin 55 HP for CFRP

A two-component epoxy resin adhesive S&P Resin 55 HP [61] (having a translucent yellow appearance) that is mating with the S&P C-sheet 240 was used in the wet lay-up process of CFRP sheets. Table 1 lists the main mechanical properties of the adhesive.

2.4. Steel plates

Steel plates [25] with an elastic modulus, yield strength, and ultimate strength of 205 GPa, 421 MPa, and 526 MPa, respectively, as shown in Table 1, were used in the tests.

3. Experimental study

3.1. Specimens and test matrix

The experimental program was designed to investigate the repair effect of adhesively bonded Fe-SMA and Fe-SMA/CFRP patches with different patch lengths. Fig. 3 illustrates the specimen configurations and Table 2 summarizes the test matrix. The steel plates had a through-thickness notch at the plate center (Fig. 3a) and precracks of ≥ 1 mm (see Section 3.2.1 for the details of precracks). Two categories of repair patches were involved, i.e., bonded Fe-SMA strips (Fig. 3b) and bonded Fe-SMA/CFRP patches (Fig. 3c), respectively. For those repaired with Fe-SMA strips, Fe-SMA strips were symmetrically bonded on both sides of the steel plates using adhesive SikaPower-1277, covering the notch and precracks; subsequently, the middle zones of the Fe-SMA strips were activated to generate prestress (Fig. 3b). For those repaired with Fe-SMA/CFRP patches, Fe-SMA strips were bonded on both sides and subsequently activated, and lastly, additional CFRP sheets were bonded using the mating adhesive (i.e., S&P C-sheet 240 and S&P Resin 55 HP), covering the Fe-SMA strips (Fig. 3c).

A compact repair patch is desirable for practical application to minimize material costs and enhance its applicability in limited spaces. However, patch length affects bond capacity, Fe-SMA prestress level, and stress distribution in the parent structures. Therefore, as an important parameter to optimize, patch length was investigated.

In all repaired specimens, Fe-SMA strips had the uniform width of 50 mm and thickness of 1.5 mm (i.e., W_{SMA}=50 mm and t_{SMA}=1.5 mm), while the length L_{SMA} varied from 100 mm to 500 mm, as shown in Table 2. The middle zone, with a half length of the Fe-SMA strip, was activated (i.e., activation length $L_{act} = L_{SMA}/2$) while the two ends were working as anchorage during activation (i.e., anchorage length $L_{anc} = L_{SMA}/4$). The CFRP sheets fully covered the Fe-SMA strips, with a margin of 20 mm in each edge. Consequently, all CFRP sheets had a fixed width of 90 mm (i.e., W_{CFRP}=90 mm), while the CFRP length L_{CFRP} varied with the Fe-SMA length (i.e., $L_{CFRP} = L_{SMA}$+40 mm).

According to previous lap-shear tests [55,62], the effective bond length L_{eff} of Fe-SMA-to-steel joints bonded with SikaPower-1277 was approximately 120 mm. Therefore, the specimen with 500 mm long Fe-SMA strips represented a sufficient length: the anchorage length was more than the effective bond length (i.e., $L_{anc} \geq L_{eff}$) and the bond length from the cracked section to the end of Fe-SMA strip (i.e., $L_{SMA}/2$) was more than double the effective bond length (i.e., $L_{SMA}/2 \geq 2L_{eff}$). In contrast, the specimen with 100 mm long Fe-SMA strips represented an

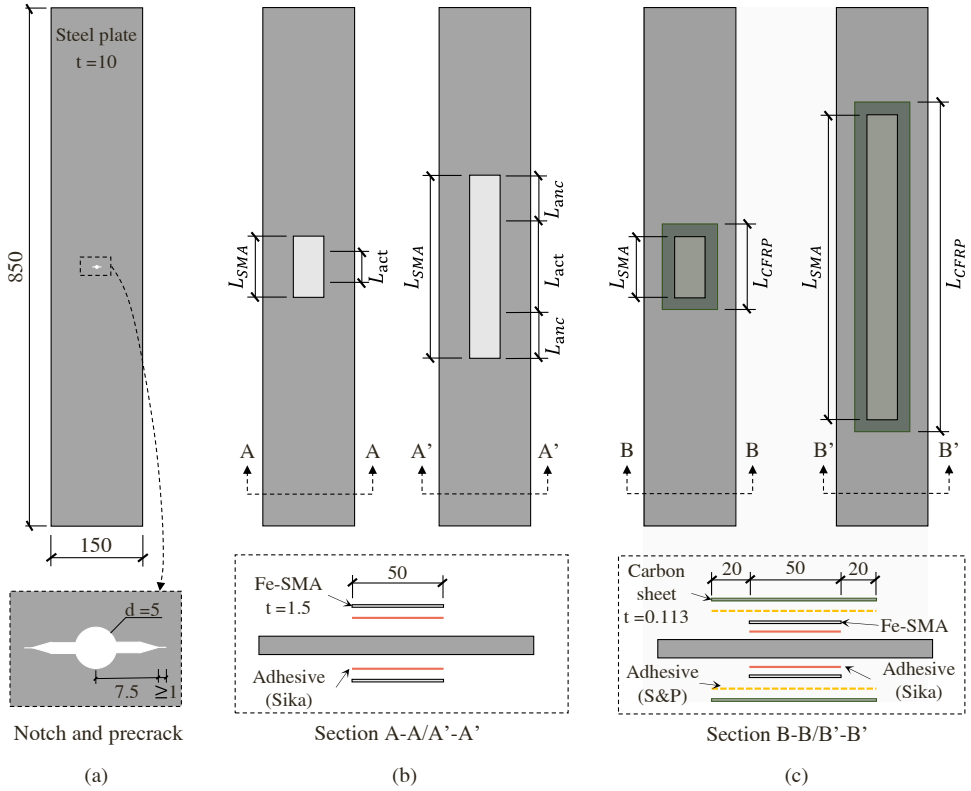

Fig. 3. Specimen configuration. (a) Reference steel plate (without repair) showing notch and precrack. (b) Repair using bonded Fe-SMA strips with different lengths. (c) Repair using bonded Fe-SMA/CFRP patches with different lengths. L_{SMA}: Fe-SMA strip length. L_{act}: activation length. L_{anc}: anchorage length. L_{CFRP}: CFRP sheet length. Unit: mm.

Table 2
Test matrix.

Specimens[a]	Precrack length[b](mm)	Repair	L_{SMA} (mm)	W_{SMA} (mm)	L_{act} (mm)	L_{anc} (mm)	L_{CFRP} (mm)	W_{CFRP} (mm)
Reference	1.40	No	-	-	-	-	-	-
S−100	1.70	Fe-SMA	100	50	50	25	-	-
S−300	1.05	Fe-SMA	300	50	150	75	-	-
SC−100	1.55	Fe-SMA+CFRP	100	50	50	25	140	90
SC−200	1.45	Fe-SMA+CFRP	200	50	100	50	240	90
SC−300	1.65	Fe-SMA+CFRP	300	50	150	75	340	90
SC−500	1.75	Fe-SMA+CFRP	500	50	250	125	540	90

[a] In the specimen labels, S indicates repair with Fe-SMA strips whereas SC indicates repair with Fe-SMA/CFRP patches, and the subsequent number indicates the Fe-SMA length (i.e., L_{SMA}).
[b] Average value of precrack lengths measured at both notch tips through travelling microscope.

extremely compact configuration: $L_{SMA}/2 \leq L_{eff}/2$ and $L_{anc} \leq L_{eff}/4$ such that the bond capacity was a concern whereas the prestress effect was expected to be localized.

3.2. Experimental procedures

The experimental procedures included precracking steel plates, bonding Fe-SMA strips, activation of Fe-SMA, bonding CFRP sheets (for some specimens), and fatigue tests.

3.2.1. Precracking steel plates

For all steel plates, a through-thickness notch was cut using the electrical discharge machining. Subsequently, they were fatigue loaded in the computer-controlled servo hydraulic fatigue testing machine (Walter+bai testing frame, Type LFV 500-HH) to introduce natural sharp precracks at the notch tips (Fig. 3a and Fig. 4).

The precracking procedure followed the specification ASTM E647–22 [64] and previous studies [25,38,40]. The beach marking technique was adopted, which was achieved by a specific loading regime as shown in Fig. 5. An interval of N_1 cycles of full-amplitude fatigue loading was applied, followed by an interval of N_2 cycles of half-amplitude fatigue loading while the maximum stress was kept constant, and such intervals ($N_1 + N_2$) were repeated. The crack propagation rate decreases substantially during the half-amplitude loading intervals, generating a distinct texture on the fracture surface. Such textures formed at known cycles can be identified, allowing for tracing the crack lengths at specific fatigue cycles after specimen fracture.

For precracking, a load with the stress range of $\Delta\sigma$=75 MPa, stress ratio of R=0.2, and loading frequency of f=15 Hz was applied to the notched bare steel plates (i.e., the full- and half-amplitude loads corresponded to (σ_{min}, σ_{max})=(18.75, 93.75) MPa and ($\sigma_{min,b}$, σ_{max})=(56.25, 93.75) MPa, respectively). N_1 and N_2 were 50,000 and 25,000, respectively, and $N_1 + N_2$ were repeated four times (i.e., in total 200,000 full-amplitude cycles).

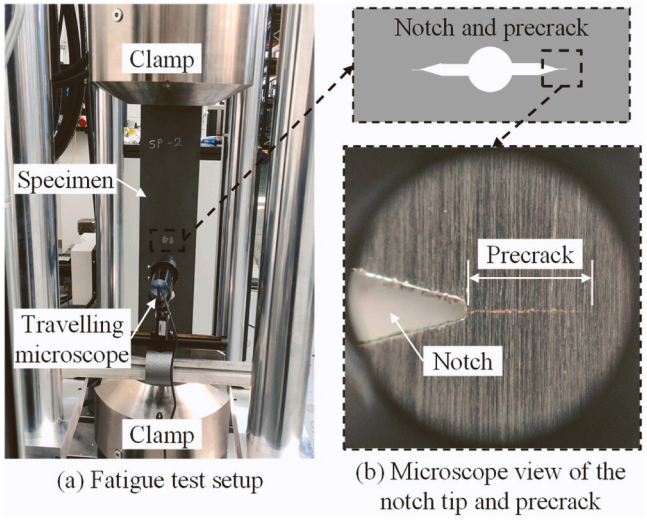

Fig. 4. (a) Fatigue test setup. (b) Microscope view of the notch tip and precrack.

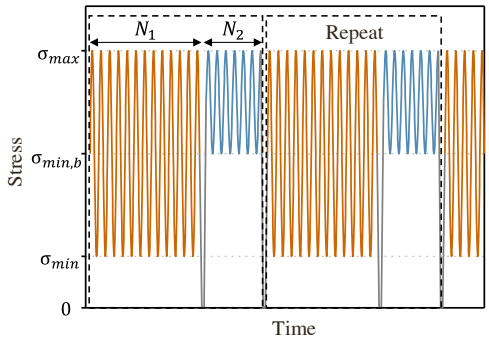

Fig. 5. Loading regime in the beach-marking technique.

According to ASTM E647–22 [64], a minimum precrack length of 1.0 mm is required. A travelling microscope with a resolution of 0.01 mm was used to measure the precrack length (Fig. 4), and the measured precrack lengths (the average value of those measured from the surface at both notch tips) are listed in Table 2.

3.2.2. Bonding Fe-SMA strips

Previous studies [55,62,65] investigated surface preparation methods for Fe-SMA to ensure integrity and durability of bonded joints. In this study, the surface preparation involved cleaning Fe-SMA strips and steel plates with acetone, followed by sandblasting. Adhesive SikaPower-1277, which is viscous and contains 0.3 mm glass beads itself [58], was applied via a cartridge. The Fe-SMA strips and steel plates were firmly joined using G-clamps, tightened to remove surplus adhesive, such that the adhesive thicknesses were ≥0.3 mm. Curing took place in a climate-controlled room (20 ℃, 50 % relative humidity) for over one week. Fig. 6a shows the specimens with bonded Fe-SMA strips.

3.2.3. Activation of Fe-SMA

The electrical resistive heating technique was selected for the activation of Fe-SMA, considering its controllability, rapidity, synchronism, and accuracy [63,66]. Fig. 6b shows the activation setup and Fig. 7a illustrates the schematic diagram. Specimens were placed on roller supports. Four customized copper connectors, each having a contact area of 50 mm×10 mm with the Fe-SMA strips (i.e., the same width as the Fe-SMA strips), were fixed by the G-clamps with good isolation. The Fe-SMA strips on both sides were connected as a series circuit (Fig. 7a). A computer-controlled electric power supply provided a current of 450 A (i.e., a current density of 6 A/mm^2).

The Fe-SMA strips were heated to a target activation temperature of 180 ℃. During activation, six thermocouples monitored the

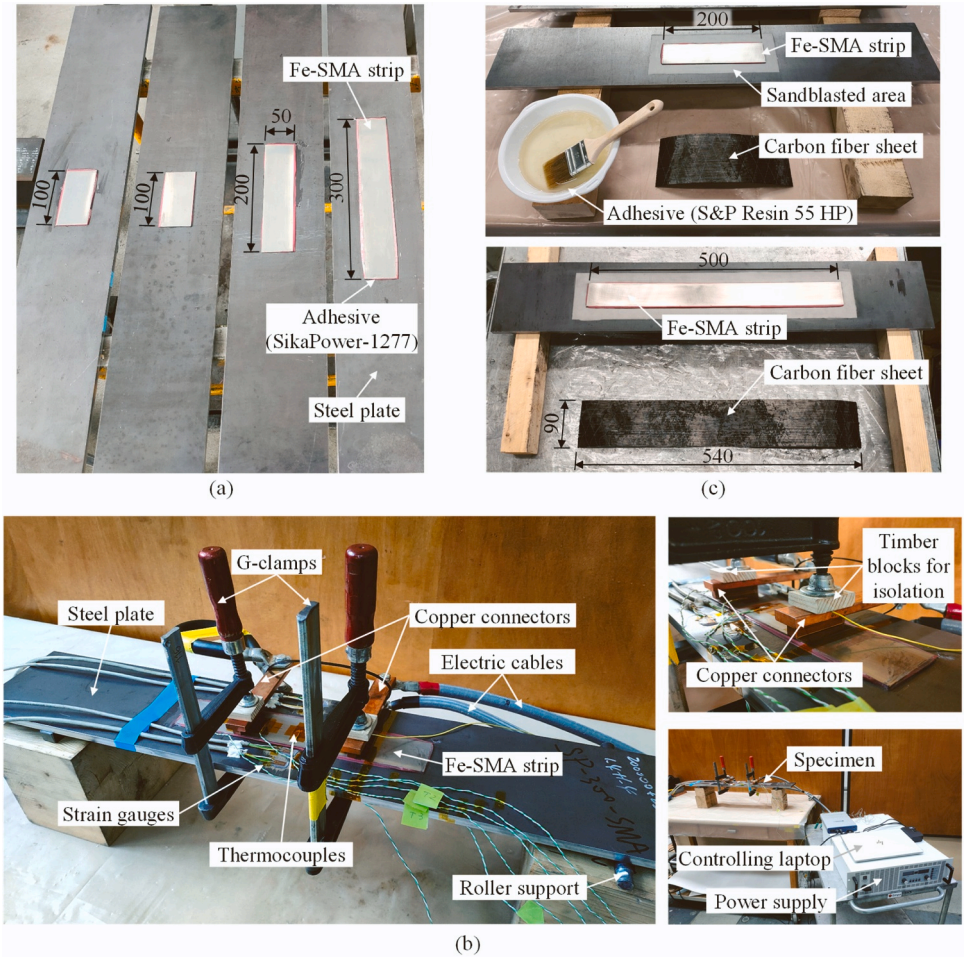

Fig. 6. (a) Bonding Fe-SMA strip. (b) Activation of Fe-SMA using electrical resistive heating. (c) Bonding CFRP sheet after activation of Fe-SMA. Unit: mm.

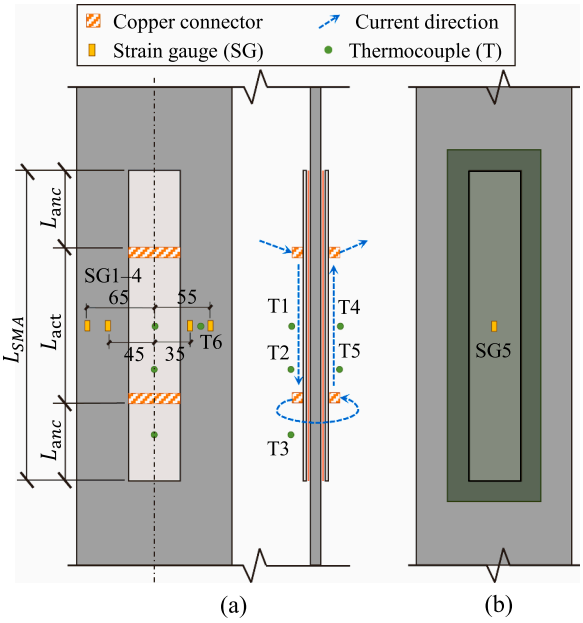

Fig. 7. (a) Instrumentations and diagram for activation of Fe-SMA. (b) Strain gauge in fatigue test. Unit: mm.

temperatures: T1—T2 and T4—T5 for the activation zones of Fe-SMA strips on both sides, respectively; T3 for the anchorage zone of Fe-SMA strip; whereas T6 for the steel plate (Fig. 7a). When the temperature measured by any of the four thermocouples (i.e., T1, T2, T4, and T5) reached 180 °C, the power supply switched off automatically. Then the specimens cooled in air to room temperature. Four strain gauges (SG1—4 in Fig. 7a) on the steel plate measured strains caused by Fe-SMA prestress. The strain gauges were deployed along the steel plate width at the mid-section, two on each lateral side of the central axis; while they were positioned at different distances to the central axis, specifically at 35, 45, 55, and 65 mm, respectively. Owing to specimen symmetry, the strains measured on one side were mirrored to the other side.

Two major concerns were to be addressed in the activation test, particularly for the activation of 100 mm long Fe-SMA strips: (1) During the activation, the high temperature of the activation zone might transfer to the anchorage zones and cause adhesive softening of the anchorage zones, resulting in anchorage failure [63]; (2) The development of prestress might exceed the capacity of anchorage zones with short bond length, potentially causing premature debonding.

3.2.4. Bonding CFRP sheets

For the specimens repaired with Fe-SMA/CFRP patches, CFRP sheets were bonded after the Fe-SMA strips were activated. Fig. 6c shows the process of bonding CFRP. To facilitate CFRP bonding, the steel plate surfaces underwent sandblasting to eliminate oxidation and enhance roughness; however, the Fe-SMA strip surfaces were ground using sandpapers instead of sandblasting to minimize potential impact on existing Fe-SMA prestress from surface preparation. The carbon fiber

sheet (S&P C-sheet 240) saturated with the epoxy resin adhesive (S&P Resin 55 HP) was laid upon the Fe-SMA strip. After the wet lay-up process, the specimens cured in the climate-controlled room for over one week.

3.2.5. Fatigue test

Fatigue tests were performed on the Walter+bai testing frame (Fig. 4a) for the reference and repaired specimens. A strain gauge (SG5 in Fig. 7b) was mounted at the center of either Fe-SMA strip (for specimens repaired with Fe-SMA strips) or CFRP sheet (for specimens repaired with Fe-SMA/CFRP patches) to monitor the crack propagation. The loading schemes were designed based on the previous studies [25, 38,40] as follows. The beach marking loading regime (Fig. 5) was employed with N_1 and N_2 set as 50,000 and 25,000, respectively. A load level with the stress range of $\Delta\sigma$=90 MPa, stress ratio of R=0.2, and loading frequency of f=15 Hz (for N_1 phase) was applied. If fatigue cracks propagated, the fatigue load continued until specimen failure. If crack propagation was not observed over 3 million cycles, as determined from SG5 measurement, the load level was then increased to the stress range of $\Delta\sigma$=105 MPa while maintaining the stress ratio and frequency, and the specimen was loaded until failure.

4. Experimental results

4.1. Activation results

Fig. 8 shows specimen temperature histories during the activation process (i.e., the heating and cooling process). In approximately 20—60 s, the electricity heated the Fe-SMA activation zone to the target temperature of 180 ℃. For specimens S-100 and SC-100 (Fig. 8a and c), when the maximum temperature reached 180 ℃, some thermocouples at the activation zones showed temperatures ≤140 ℃ (even ≤100 ℃), indicating non-uniform temperature fields of the activation zones. With increased Fe-SMA strip length, the temperature fields of the activation zones appeared to be more uniform. After heating, the specimens were placed for several hours to completely cool to room temperature. Throughout activation, steel plates reached maximum temperatures of 32—68 ℃ across all specimens. The maximum temperatures of Fe-SMA anchorage zones across all specimens were 36—45 ℃, remaining below the adhesive glass transition temperature T_g=67 ℃.

Fig. 9a and b show the typical strain histories of steel plates during activation. To ensure equipment safety, strain gauge connections were intentionally severed when applying electric current to the Fe-SMA

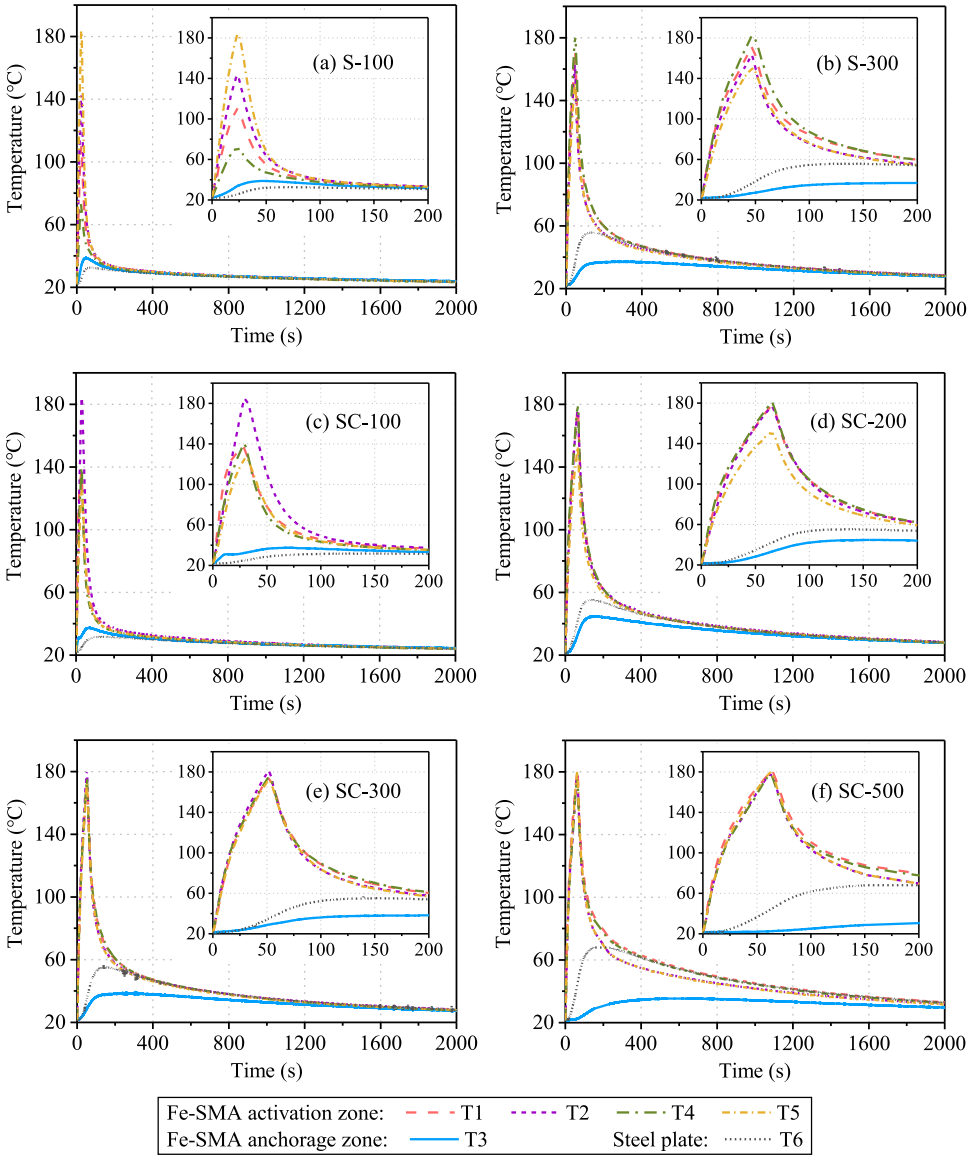

Fig. 8. Temperature histories of different thermocouples during the activation process. (a) S-100. (b) S-300. (c) SC-100. (d) SC-200. (e) SC-300. (f) SC-500.

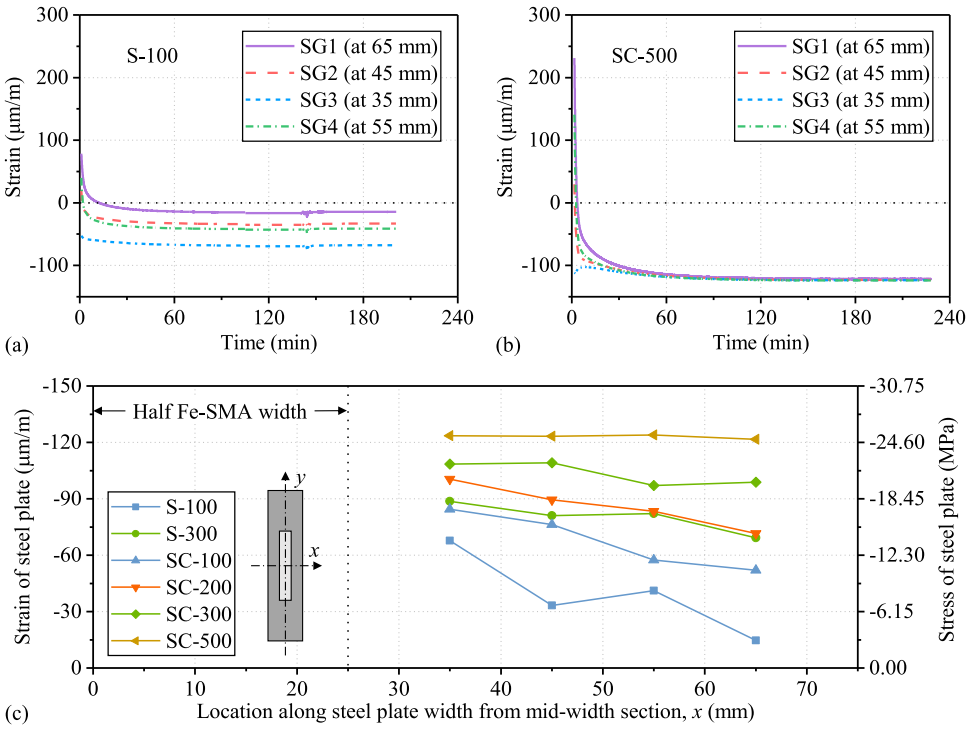

Fig. 9. Experimentally measured strains of steel plates throughout activation. (a) Strain histories of S-100. (b) Strain histories of SC-500. (c) Final strains at the end of activation process for all specimens.

strips; consequently, only strain histories during the cooling process were recorded, omitting the initial strain histories during the heating process. Meanwhile, as the adopted strain gauges were temperature self-compensated, their strain readings directly reflected deformation [67, 68]. Initially, tensile strains existed in steel plates, arising from the thermal deformations. Upon cooling, only compressive strains remained, indicating the effect of Fe-SMA prestress.

Fig. 9c and Table 3 summarize the final strains after activation and corresponding stresses for all specimens. The final strains were compressive for all specimens. In general, an increased strain gradient along the steel plate width was observed for decreased Fe-SMA strip length. Section 5 will present a further analysis exploiting the measured strain data, in conjunction with numerical modelling, to estimate Fe-SMA prestresses.

The activation results addressed the two concerns outlined in Section 3.2.3 related to activating 100 mm long Fe-SMA strips. The temperatures of anchorage zones remained below T_g without additional cooling measures, and prestresses were successfully generated and sustained in the bonded Fe-SMA strips, with no occurrence of debonding.

4.2. Fatigue test results

Table 4 summarizes the fatigue test results, wherein the fatigue cycles N only counted the full-amplitude cycles. Fig. 10a shows the evolution of the maximum strain reading of SG5 on Fe-SMA strip or CFRP sheet, reflecting crack behavior (i.e., propagation or arrest). During fatigue loading, an increasing maximum strain indicated crack propagation, while a constant maximum strain suggested crack arrest.

Specimen SC-100 exhibited minimal strain change (Fig. 10a) after 3.315×10^6 fatigue cycles under the load level of $\Delta\sigma$=90 MPa; therefore, it was regarded as fatigue crack arrest. Thereafter, SC-100 was subjected to an increased load level of $\Delta\sigma$=105 MPa, and failure occurred after 1.167×10^6 cycles. The other specimens all failed under the load level of $\Delta\sigma$=90 MPa.

Fig. 11 shows the failure modes and fracture surfaces of the repaired specimens after fatigue tests. Failure modes varied depending on the patch length. The failure modes of specimens with $L_{SMA} \leq 200$ mm were featured by debonding, wherein Fe-SMA strips were pulled off the steel plates (Fig. 11a, c, and d). However, specimens with $L_{SMA} \geq 300$ mm experienced Fe-SMA strip fracture accompanied with partial debonding (Fig. 11b, e, and f). In addition, CFRP fracture with partial debonding was observed across all specimens repaired with Fe-SMA/CFRP patches.

A postmortem analysis of the specimens was conducted to gain insights into crack growth behavior. Fig. 10b summarizes the $a - N$ curves, where a is the crack length from notch center to crack tip along the mid-thickness axis, obtained through the beach marks on the fracture

Table 3
Final strain readings and corresponding stresses in the steel plates at the end of activation process.

Specimens	Strain gauges at different locations							
	35 mm		45 mm		55 mm		65 mm	
	Strain (μm/m)	Stress (MPa)	Strain (μm/m)	Stress (MPa)	Strain (μm/m)	Stress (MPa)	Strain (μm/m)	Stress (MPa)
S−100	−67.7	−13.9	−33.2	−6.8	−41.1	−8.4	−14.6	−3.0
S−300	−88.7	−18.2	−81.1	−16.6	−82.1	−16.8	−69.2	−14.2
SC−100	−84.4	−17.3	−76.3	−15.6	−57.4	−11.8	−52.0	−10.7
SC−200	−100.5	−20.6	−89.4	−18.3	−83.4	−17.1	−71.6	−14.7
SC−300	−108.5	−22.3	−109.1	−22.4	−97.1	−19.9	−98.8	−20.3
SC−500	−123.5	−25.3	−123.2	−25.3	−123.9	−25.4	−121.6	−24.9

Table 4
Fatigue test results.

Specimens	Stress range, $\Delta\sigma$ (MPa)	Fatigue cycles, N (million)	Fatigue life improvement	Phenomena
Reference	90	0.374	-	-
S−100	90	1.579	4.2	Failure mode A[a]
S−300	90	1.853	5.0	Failure mode B[b]
SC−100	90	3.315	∞	Crack arrest[c]
	105	1.167	3.1	Failure mode C[d]
SC−200	90	2.228	6.0	Failure mode C
SC−300	90	2.165	5.8	Failure mode D[e]
SC−500	90	2.041	5.5	Failure mode D

[a] Failure mode A: Fe-SMA debonding.
[b] Failure mode B: Fe-SMA fracture and partial debonding.
[c] Crack arrest: indicated by a stable strain measurement throughout 3.315×10^6 fatigue cycles.
[d] Failure mode C: Fe-SMA debonding + CFRP fracture and partial debonding.
[e] Failure mode D: Fe-SMA fracture and partial debonding + CFRP fracture and partial debonding.

surfaces (Fig. 11), and N is the fatigue cycles counting the applied full-amplitude cycles (without counting half-amplitude cycles). Fig. 10c illustrates crack growth rate da/dN versus crack length a. The repaired specimens exhibited substantially extended fatigue lives and reduced crack growth rates compared to the reference specimen.

Fig. 10d plots the fatigue lives of all specimens. After repairing with Fe-SMA strips, the fatigue lives of S-100 and S-300 were improved by 4.2 and 5.0 times, respectively, compared to the reference specimen. SC-100 that was repaired with 100 mm long Fe-SMA/CFRP patches achieved crack arrest under the load level of $\Delta\sigma$=90 MPa. The other specimens repaired with Fe-SMA/CFRP patches showed 5.5–6.0 times improvement in fatigue lives. All repaired specimens had significantly enhanced fatigue lives, demonstrating the effectiveness of the repair solutions. Specimens with Fe-SMA/CFRP repair exhibited further increases in fatigue lives than those with Fe-SMA repair, substantiating the contribution of CFRP overlay in retarding fatigue crack growth.

Moreover, no decreasing trend of repair effectiveness was observed when the Fe-SMA strip length decreased from 500 mm to 100 mm (Fig. 10d), despite the transition of failure modes (Fig. 11). In contrast, SC-100, with the most compact Fe-SMA/CFRP repair patch, showed the best performance. Therefore, we can conclude that the Fe-SMA strip length can be as short as 100 mm and the repair patch can still work effectively. The mechanism will be further discussed in Section 5.

5. Analysis

Finite element (FE) models were established, alongside experimental measurements, to interpret outcomes that were not directly measurable, such as Fe-SMA prestress and stress intensity factor (SIF) at crack tip. This approach enabled a comprehensive analysis of the experimental results.

5.1. Finite element (FE) modeling

Fig. 12 shows the FE model of specimen SC-100, developed in Abaqus/CAE 6.16 (the other specimens were modelled similarly). Based on structural symmetry, only one-eighth of the structure was established. The steel plate was modeled using hexahedral C3D20R element, with refined mesh at the crack zone, wherein elements around the crack tip subtended an angle of 10° as recommended in Abaqus Analysis User's Guide [69]. The crack was modeled using the "Interaction → Special → Crack" command in Abaqus. The crack tip was 1 mm from the notch tip. The crack tip and its extension direction were designated as shown in Fig. 12, and the feature of half-crack model on the symmetry plane was selected. The SIFs of the crack were requested as history outputs.

The Fe-SMA strip was modeled using hexahedral C3D20R element, while the adhesive layer for bonding Fe-SMA (adhesive layer-1 in

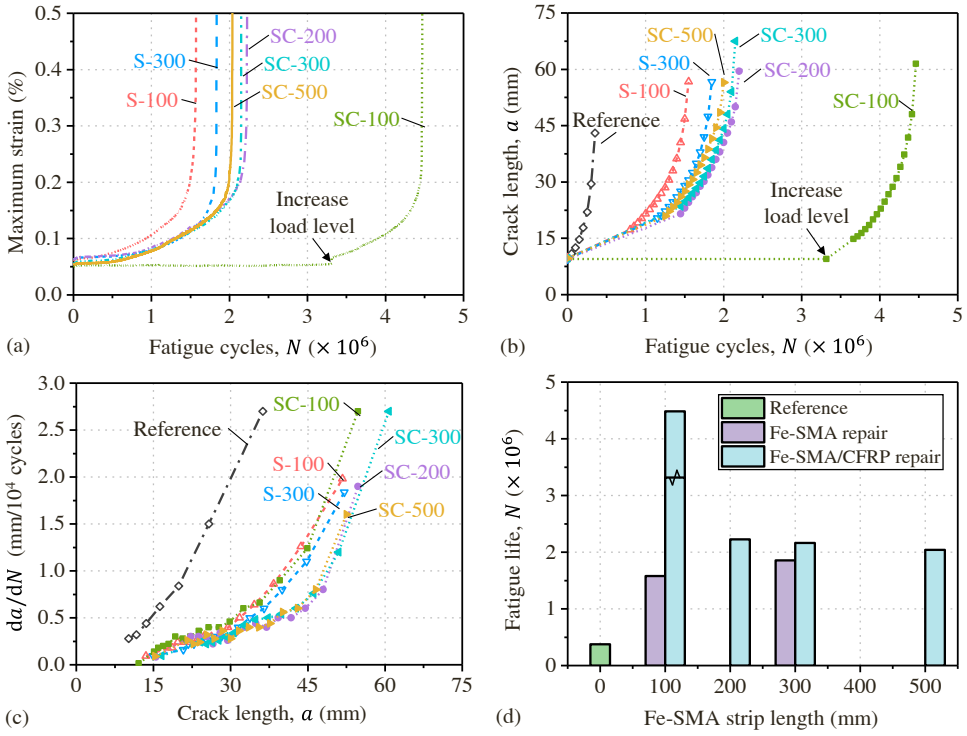

Fig. 10. Fatigue behavior. (a) Evolution of the maximum strain reading of SG5 on Fe-SMA strip or CFRP sheet. (b) Fatigue crack growth behavior. (c) Crack growth rate. (d) Fatigue lives of all specimens.

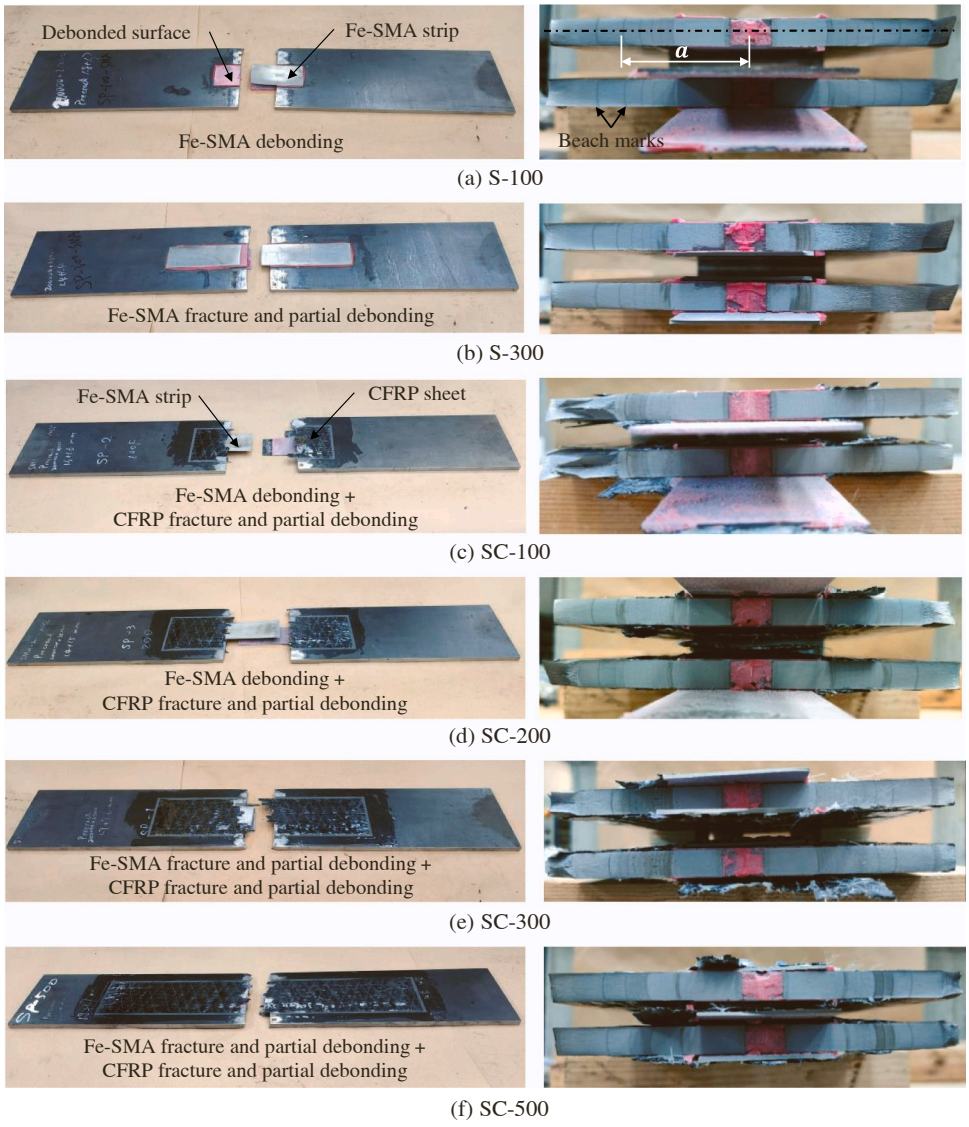

Fig. 11. Failure modes and fracture surfaces of specimens after fatigue tests. (a) S-100. (b) S-300. (c) SC-100. (d) SC-200. (e) SC-300. (f) SC-500.

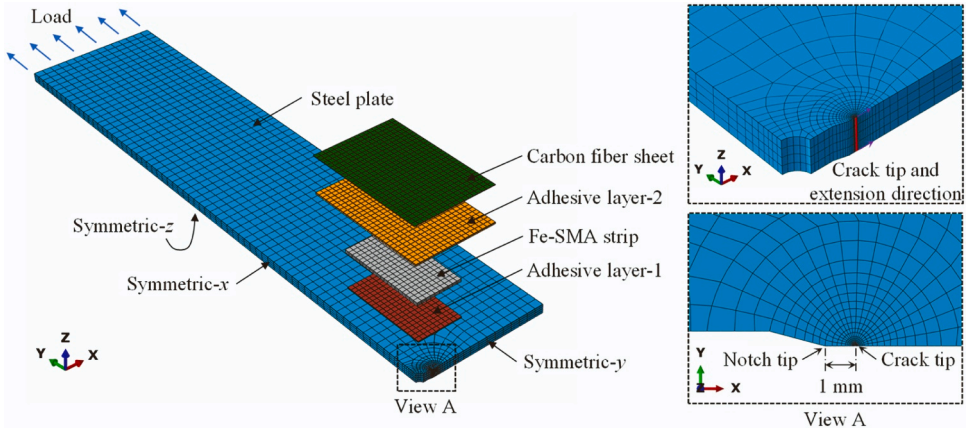

Fig. 12. Finite element (FE) model of SC-100.

Fig. 12) was modeled using cohesive element COH3D8. The thickness of Fe-SMA strip was 1.5 mm (Table 1) and was meshed as two layers of elements. The adhesive layer-1 was assumed to be 0.5 mm thick and was meshed as a single layer of element as required for cohesive elements [70]. Similarly, the bonded CFRP sheet was modeled separately, comprising an adhesive layer (adhesive layer-2 in Fig. 12) and a carbon fiber sheet layer. The thickness of adhesive layer-2 was assumed to be 0.8 mm according to an estimated adhesive consumption of

600—800 g/m^2 [57], and it was also modeled as a single layer of cohesive element COH3D8. The carbon fiber sheet with a thickness of 0.113 mm (Table 1) was modeled as a layer of hexahedral C3D20R element. Mesh sizes of Fe-SMA, carbon fiber sheet, and two adhesive layers along both length and width (x and y directions) were set at 2.5 mm, based on a mesh sensitivity analysis.

To facilitate deriving prestress and applying linear elastic fracture mechanics, all materials were defined as linear elastic, with their elastic moduli shown in Table 1. A previous study [55] compared FE simulation results of Fe-SMA-to-steel bonded joints with experimental results, validating that a linear elastic FE model was adequately accurate when the stress level of the Fe-SMA strip was ≤500 MPa; in this study, the stress level was also within this range. Furthermore, all materials, except carbon fiber sheet, were defined as isotropic. In contrast, the carbon fiber sheet was modeled as anisotropic, employing following engineering constants: E_1=240 GPa, E_2=E_3=15 GPa, ν_{12}=0.2, ν_{13}=ν_{23}=0.25, G_{12}=9.75 GPa, G_{13}=G_{23}=5.25 GPa, where direction-1 indicated the fiber longitudinal direction. The engineering constants were calculated referring to the properties of a carbon fiber fabric with a similar elastic modulus (230 GPa) reported in [71], adjusted by a factor of 240/230 for E_2, E_3, G_{12}, G_{13}, and G_{23}.

The corresponding surfaces between adjacent components were tied. Additionally, the lower surface of adhesive layer-2 was divided into two zones, tied to the upper surfaces of Fe-SMA strip and steel plate, respectively. Symmetric boundary conditions in the x, y, and z directions were applied to the respective planes as shown in Fig. 12. Notably, the region between the notch tip and crack tip remained unconstrained whereas the symmetric-y boundary condition was applied to the other regions on the plane.

5.2. Fe-SMA prestress

The Fe-SMA strip prestresses in the specimens were estimated based on the experimentally measured steel plate strains and FE models through following steps. (1) A predefined stress field of unit (1 MPa here) was assigned to the activation zone of Fe-SMA strip. (2) The compressive strain distribution of steel plate was consequently obtained, and it was assumed that the strain distribution had a constant shape but only the strain magnitude was variable; (3) A magnitude factor ζ was determined, which enabled the numerically obtained strain distribution after multiplying the factor to best match the experimentally measured strain data along the steel plate width; (4) Thereafter, a predefined stress field $\sigma_d = \zeta \bullet (1\ \text{MPa})$ was applied to the activation zone of Fe-SMA strip, and after stress re-distribution, the retained stress in the Fe-SMA strip was derived as the prestress σ_p.

Fig. 13a shows the final strain distributions of steel plates from FE models, aligning with the experimental strain data (strains near the crack tip with numerical singularity are excluded). Table 5 lists the designated predefined stress field σ_d and obtained Fe-SMA prestress σ_p for each specimen. The difference between σ_d and σ_p indicated the prestress loss due to structural compliance. The decreased Fe-SMA length exacerbated the prestress loss, evident by σ_p/σ_d in Table 5, consistent with the analytical estimations in [46]. Ultimately, the

Table 5
Summary of numerical results of Fe-SMA prestress and stress intensity factor (SIF).

Specimens	σ_d (MPa)	σ_p (MPa)	σ_p/σ_d (%)	$\Delta K_{I,eff}$ (N/mm$^{3/2}$)	
				$\Delta\sigma$=90 MPa	$\Delta\sigma$=105 MPa
Reference	-	-	-	453.4	-
S−100	215.4	153.6	71.3	286.3	-
S−300	200.7	179.8	89.6	360.1	-
SC−100	331.6	236.5	71.3	193.2	269.7
SC−200	253.1	215.9	85.3	295.3	-
SC−300	257.1	230.4	89.6	324.7	-
SC−500	276.1	253.9	92.0	340.8	-

σ_d: designated predefined stress field. σ_p: Fe-SMA prestress. $\Delta K_{I,eff}$: effective mode I SIF range. $\Delta\sigma$: stress range of fatigue load.

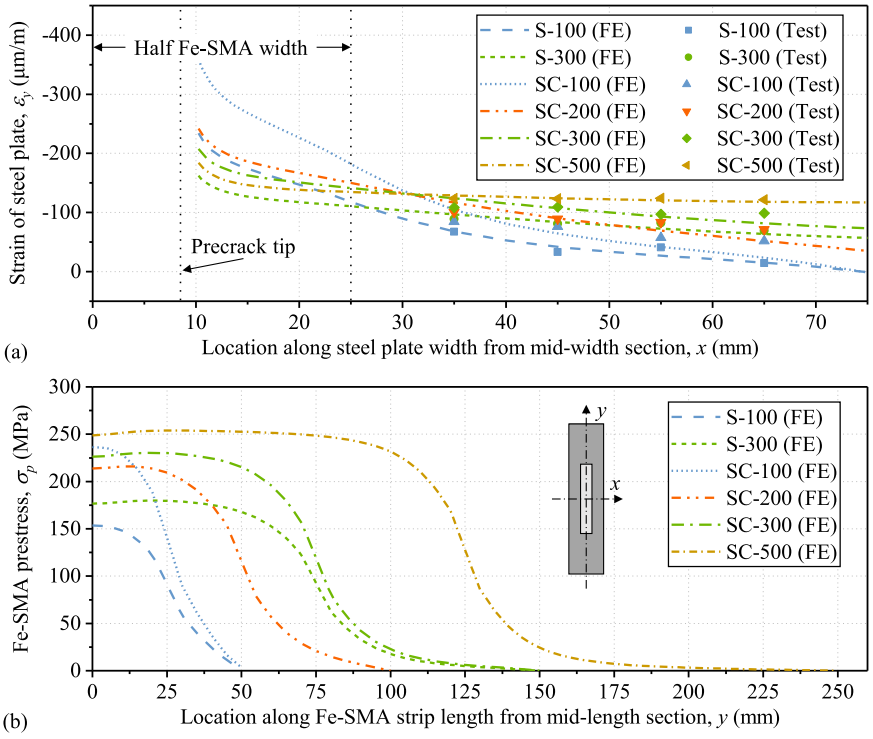

Fig. 13. Analysis of steel plate strain and Fe-SMA prestress. (a) Strain distribution of steel plate from numerical analysis along with experimental strain measurements. (b) Fe-SMA prestress distribution from numerical analysis.

Fe-SMA prestresses were estimated to range from 153.6 to 253.9 MPa, wherein S-100 and SC-500 exhibited the lowest and highest Fe-SMA prestresses, respectively. Notably, although SC-100 was applied with the highest predefined stress field σ_d, its final prestress σ_p was not the highest because of relatively high prestress loss.

Fig. 13b illustrates Fe-SMA prestress distributions along their longitudinal half-lengths. Ideally, specimens having the same Fe-SMA lengths (i.e., S-100 and SC-100, S-300 and SC-300) were nominally identical in the activation process (no CFRP at that time). However, differences in their estimated prestresses were observed (compare curves with the same colors in Fig. 13b). Such difference in the prestress was attributed to two major factors, aside from inherent test randomness. (1) The electric current in the Fe-SMA strip was not uniformly distributed, as reflected by the non-uniform temperatures measured during activation (Fig. 8). (2) Potential bending effects due to actual structural asymmetry were neglected by the analysis based on nominal symmetry.

5.3. Stress intensity factor (SIF) at crack tip

The SIF was calculated based on the FE models to analyze the crack behavior. Fig. 14 illustrates the evolution of mode I SIF (K_I) with externally applied stress σ. Note that K_I at the crack tip varied slightly along the steel plate thickness, and the value presented in Fig. 14 was derived from points located at a distance of 3/8 thickness from the free surface. All curves in Fig. 14 are linear because of the linear elastic assumption for all materials in the FE models. The curves have different origins ($K_{I,\sigma=0}$) and slopes ($\frac{dy}{dx}$), as listed in Fig. 14, indicating the effects of prestress and load sharing from the repair patches, as elaborated below.

For the reference specimen (i.e., bare steel plate with central crack), its SIF at the crack tip can be estimated analytically through Eq. 1 — Eq. 2 [25,64].

$$K_I = f(a,w)\sigma \tag{1}$$

$$f(a,w) = \sqrt{\pi a \sec\frac{\pi a}{w}} \tag{2}$$

where a is the crack length (here, a=8.5 mm, the initial crack length from crack tip to the Symmetric-x plane in Fig. 12) and w is the width of steel plate (w=150 mm). When the externally applied stress σ was 112.5 MPa, the analytically calculated K_I was 586.0 N/mm$^{3/2}$. In the FE model of reference specimen, the SIFs K_I at the crack tip along the steel plate thickness ranged from 548.1 to 629.7 N/mm$^{3/2}$ at the same stress level of 112.5 MPa. The analytical and numerical results showed good agreement.

The origins ($K_{I,\sigma=0}$) of the curves in Fig. 14 indicated the effect of Fe-SMA prestress on the SIF at crack tip. The reference specimen had $K_{I,\sigma=0}$=0, whereas all repaired specimens had negative values of $K_{I,\sigma=0}$. In specimens SC-100 to SC-500, similar Fe-SMA prestress levels were obtained (Table 5), but $K_{I,\sigma=0}$ increased (having smaller absolute values) with the patch length, with SC-100 having the lowest $K_{I,\sigma=0}$ (Fig. 14). This was because a shorter patch length led to a more concentrated compression, as shown by the compressive strain distribution in Fig. 13a.

The slopes ($\frac{dy}{dx}$) of the curves in Fig. 14 indicated the effect of bonded Fe-SMA strips and CFRP sheets in load sharing. In general, bonding Fe-SMA strips reduced the slope, and bonding Fe-SMA/CFRP patches further reduced it (e.g., S-100 and SC-100 reduced the slope from 5.60 to 4.38 and 4.31, respectively). Meanwhile, shorter patches exhibited a slightly greater reduction in the slope (e.g., the slope decreased from 4.58 to 4.31 for specimens from SC-500 to SC-100).

The crack behavior (i.e., whether the crack arrests or propagates) can be predicted through Eq. 3 — Eq. 4 [25].

$$\begin{cases} \text{Crack arrest, if} \Delta K_{I,eff} < \Delta K_{I,th} \\ \text{Crack propagate, if} \Delta K_{I,eff} > \Delta K_{I,th} \end{cases} \tag{3}$$

$$\Delta K_{I,eff} = U\Delta K_I \tag{4}$$

$$\begin{cases} \Delta K_I = K_{I,max} - K_{I,min}, \text{if} K_{I,min} > 0 \\ \Delta K_I = K_{I,max} - 0, \text{if} K_{I,min} \le 0 \end{cases} \tag{5}$$

where $\Delta K_{I,eff}$ is the effective mode I SIF range considering crack closure effect as per Eq. 4; $\Delta K_{I,th}$ is the threshold mode I SIF range, being a characteristic value of the material; U accounts for crack closure effect and U=0.9 was experimentally obtained by Hosseni et al. [25] for the steel plates same as those used in this study, through measuring crack opening force; ΔK_I is the mode I SIF range which can be calculated through Eq. 5 based on the numerical K_I results shown in Fig. 14; $K_{I,max}$ and $K_{I,min}$ are the maximum and minimum mode I SIFs corresponding to the applied stress range $\Delta\sigma$, respectively.

Table 5 lists the calculated results of effective mode I SIF ranges $\Delta K_{I,eff}$ of the specimens. Hosseini et al. [25] and Li et al. [42] examined crack propagation behavior of the steel plates (same as those used in this study) under different fatigue loading levels, wherein they estimated the threshold mode I SIF range $\Delta K_{I,th}$ of the steel plates to fall between 200 and 285 N/mm$^{3/2}$. Therefore, a prediction of crack propagation can be made when $\Delta K_{I,eff}$ is larger than or close to 285 N/mm$^{3/2}$, while crack arrest is expected when $\Delta K_{I,eff}$ is less than 200 N/mm$^{3/2}$. Fig. 15 shows the $\Delta K_{I,eff}$ of the specimens compared with the two boundary values of $\Delta K_{I,th}$. According to Fig. 15, the $\Delta K_{I,eff}$ of SC-100 at $\Delta\sigma$=90 MPa was 193.2 N/mm$^{3/2}$, suggesting crack arrest; while its $\Delta K_{I,eff}$ increased to 269.7 N/mm$^{3/2}$ at $\Delta\sigma$=105 MPa, suggesting crack propagation. In contrast, for all other specimens, their $\Delta K_{I,eff}$ at $\Delta\sigma$=90 MPa suggested crack propagation.

The crack behavior deduced through the FE simulation and SIF analysis was consistent with the fatigue test results. This mutual consistency confirms the accuracy of experimentally measured strains, the

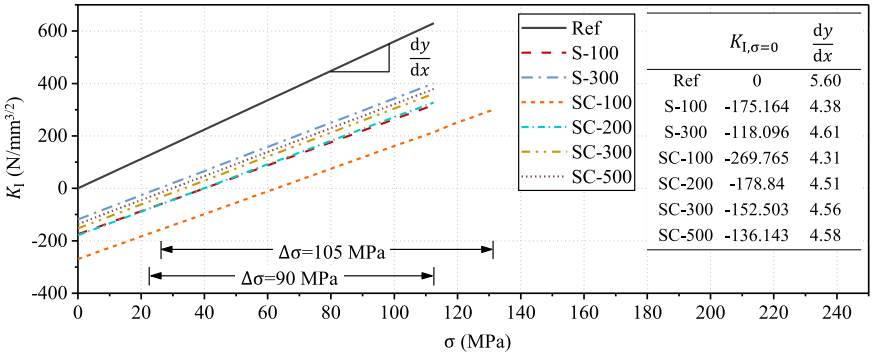

Fig. 14. Numerical results of mode I stress intensity factor K_I versus externally applied stress σ.

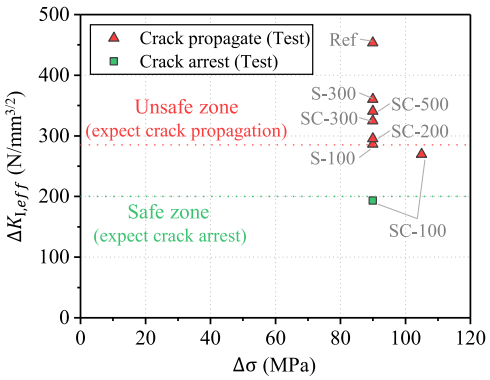

Fig. 15. Analysis of crack behavior through effective mode I stress intensity factor range $\Delta K_{I,eff}$. SC-100 experienced two load levels of $\Delta\sigma$=90 and 105 MPa, respectively; the other specimens were tested at $\Delta\sigma$=90 MPa.

validity of estimated Fe-SMA prestress results, and the reliability of the fatigue tests. The analysis in this subsection further substantiates and quantifies the beneficial effects from the Fe-SMA prestress and the load sharing of Fe-SMA strips and CFRP sheets in mitigating SIF at crack tips, thus retarding crack propagation. Moreover, it validates that repair patches with decreased patch lengths, despite experiencing higher prestress loss, were effective in reducing SIF at crack tips and thus retarding crack propagation.

6. Design recommendations

Repair solutions for fatigue cracks should be tailored based on practical conditions, considering factors such as crack conditions (location, size, orientation, severity), parent structure details (material, geometry, accessibility, current condition), actions and environmental conditions (load, temperature, moisture, sunlight, corrosive chemicals), and design criteria (performance demand, design working life). Various techniques, such as welding repair, drilling crack-arrest holes, unbonded/bonded CFRP, and unbonded/bonded Fe-SMA strips, can be considered individually or in combination.

This study investigated using Fe-SMA and Fe-SMA/CFRP bonded patches, showcasing the effectiveness of these self-prestressing patches in extending fatigue lives of cracked steel structural details, with applicability for repair in confined spaces. In most cases, using only bonded Fe-SMA can be adequate to achieve desired repair effect through adjusting Fe-SMA dimensions, prestraining levels, and activation temperatures. The Fe-SMA/CFRP bonded patch provides an alternative with flexible CFRP sheets offering additional load-sharing and protection for Fe-SMA. Nevertheless, utilizing Fe-SMA/CFRP bonded patches involves more operational processes than using Fe-SMA or CFRP alone.

In repair solutions using Fe-SMA or Fe-SMA/CFRP bonded patches, the activation of Fe-SMA is a critical step, and several activation methods can be used, such as electric heating, handheld torches, heating air guns. Electric heating is adopted in this study, as it can be well controlled and monitored, while it requires specific equipment. In contrast, a handheld small torch is a convenient option for field applications, but its temperature control accuracy is relatively low [41,67]. The activation temperature can be determined considering required prestress level, Fe-SMA prestraining level, temperature control accuracy, and adhesive temperature resistance [67,72].

In designing repair patches, the sectional dimensions of Fe-SMA strip, length of Fe-SMA strip (i.e., activation length L_{act} + anchorage length L_{anc}), and dimensions of CFRP sheet can be adjusted through an iterative analysis process to optimize repair effect and material efficiency. This study explored extremely short Fe-SMA lengths (100 mm) and validated its feasibility and effectiveness. However, for practical application, a more conservative approach is recommended. Eq. 6 is proposed to facilitate the design of Fe-SMA lengths (partial factors are excluded).

$$L_{anc} \geq \frac{(\sigma_p + \sigma_{l,\max}) \bullet t_{SMA}}{\tau_{adh}} \tag{6}$$

where t_{SMA} is the Fe-SMA thickness; σ_p is the Fe-SMA prestress; $\sigma_{l,\max}$ is the maximum stress of Fe-SMA caused by external load; τ_{adh} is the shear strength design value of adhesive; activation length L_{act} can be designed based on repair effect.

As an example, the patches in this study can be designed as follows. The L_{act} is set at 50 mm, as the optimal crack closure effect was observed (the optimal activation length may vary under different conditions, and a FE or analytical analysis is recommended). The shear strength of adhesive SikaPower-1277 is τ_{adh}=10 MPa, corresponding to the average shear stress along the effective bond length at bond capacity, measured through lap-shear tests of Fe-SMA-to-steel bonded joints (Table 1) [55,62]. The Fe-SMA prestress is assumed as 250 MPa, with the Fe-SMA thickness of 1.5 mm. The maximum stress of Fe-SMA caused by external load (corresponding to the fatigue load $\Delta\sigma$=90 MPa) is 112.5 MPa. Therefore, L_{anc} should be ≥54.4 mm according to Eq. 6.

Furthermore, it is imperative to consider the long-term behavior, including prestress loss due to creep and relaxation, as well as capacity degradation due to corrosion and aging [50,72]. One approach to consider the long-term behavior is to incorporate a long-term coefficient in the design, while further investigations on the durability of Fe-SMA or Fe-SMA/CFRP bonded patches are needed. Additionally, a reasonable inspection, monitoring, and maintenance plan is essential to ensure continuous structural functionality and integrity.

7. Conclusions

This study explores repair strategies for lifetime extension of cracked steel structures employing adhesively bonded Fe-SMA and Fe-SMA/CFRP patches, wherein prestrained Fe-SMA strips, bonded over cracks, are activated through heating and cooling to generate prestress. Activation behavior and fatigue performances are tested and analyzed. The following conclusions are drawn:

1. Bonded Fe-SMA strips, 50 mm wide and 1.5 mm thick, with varied lengths from 100 to 500 mm, are activated to 180 ℃ using electric resistive heating technique. Fe-SMA prestresses at 153.6—253.9 MPa, estimated through experimentally measured strains and finite element (FE) simulations, are successfully generated and sustained without causing debonding issue during the activation process.
2. Repairing cracked steel plates using bonded Fe-SMA strips substantially improves the fatigue lives by 4.2—5.0 times, owing to the Fe-SMA prestresses and their load sharing. Using Fe-SMA/CFRP patches further enhances the fatigue lives, achieving extension ratios exceeding 5.5 or even achieving complete crack arrest.
3. With patch length decreasing, the failure modes transition from Fe-SMA (and CFRP) fracture for long (≥ 300 mm) patches to debonding for short (≤ 200 mm) patches, while all patches remain effective in fatigue life extension. The 100 mm long Fe-SMA/CFRP patch exhibits an optimal performance for lifetime extension, completely arresting cracks under a fatigue load with a stress range of $\Delta\sigma$=90 MPa and a stress ratio of 0.2.
4. The repair mechanism is investigated based on FE models. Numerical analysis quantifies the effect of prestress and load sharing from the repair patches on reducing the stress intensity factors (SIFs) at crack tips. Compact repair patches, despite experiencing relatively high prestress loss, induce concentrated compression at crack tips, resulting in a significant reduction in SIF and enhanced repair effectiveness. Analysis of crack arrest/propagation behavior through

SIFs exhibits good consistency with fatigue test results, confirming the validity of results obtained in this study.

5. Repair patches should be tailored according to practical conditions. Design recommendations are proposed to aid decision-making and facilitate the formulation of repair solutions for cracked steel details, including activation approaches, patch configurations, and dimensions. Similar repair solutions can also be applied to concrete structures, while further studies are required to investigate the repair effectiveness of the self-prestressing patches on cracked concrete.

CRediT authorship contribution statement

Sizhe Wang: Writing – original draft, Visualization, Validation, Software, Methodology, Investigation, Formal analysis, Data curation, Conceptualization. **Qingtian Su:** Writing – review & editing, Supervision, Resources. **Xu Jiang:** Writing – review & editing, Supervision, Project administration, Funding acquisition. **Lingzhen Li:** Writing – review & editing, Validation, Investigation, Conceptualization. **Masoud Motavalli:** Writing – review & editing, Supervision, Resources, Project administration, Funding acquisition, Conceptualization. **Elyas Ghafoori:** Writing – review & editing, Supervision, Project administration, Funding acquisition, Conceptualization.

Declaration of Competing Interest

The authors declare that they have no known competing financial interests or personal relationships that could have appeared to influence the work reported in this paper.

Data availability

Data will be made available on request.

Acknowledgement

Supports from the National Natural Science Foundation of China (52278207) and China Scholarship Council (CSC) are acknowledged. The authors also acknowledge the supports from Structural Engineering Laboratory of Empa and the supports from re-fer AG, Switzerland, Sika AG, Switzerland, and S&P AG, Switzerland, for the sponsored materials for this study. The authors also acknowledge Mr. André Kupferschmid and Mr. Robert Widmann for their assistance in conducting the experiments.

References

[1] International Energy Agency. Iron and Steel Technology Roadmap: Towards more sustainable steelmaking, 2020.
[2] Ž. Domazet, Comparison of fatigue crack retardation methods, Eng. Fail. Anal. 3 (2) (1996) 137–147.
[3] J.G. Teng, T. Yu, D. Fernando, Strengthening of steel structures with fiber-reinforced polymer composites, J. Constr. Steel Res. 78 (2012) 131–143.
[4] H. Liu, R. Al-Mahaidi, X.-L. Zhao, Experimental study of fatigue crack growth behaviour in adhesively reinforced steel structures, Compos. Struct. 90 (1) (2009) 12–20.
[5] H. Liu, Z. Xiao, X.-L. Zhao, R. Al-Mahaidi, Prediction of fatigue life for CFRP-strengthened steel plates, Thin Walled Struct. 47 (10) (2009) 1069–1077.
[6] Q.Q. Yu, T. Chen, X.L. Gu, X.L. Zhao, Z.G. Xiao, Fatigue behaviour of CFRP strengthened steel plates with different degrees of damage, Thin Walled Struct. 69 (2013) 10–17.
[7] T. Chen, L. Li, N. Zhang, X. Song, Y. Hidekuma, Fatigue performance test on inclined central cracked steel plates repaired with CFRP strand sheets, Thin Walled Struct. 130 (2018) 414–423.
[8] Q.-Q. Yu, Y.-F. Wu, Fatigue retrofitting of cracked steel beams with CFRP laminates, Compos. Struct. 192 (2018) 232–244.
[9] T. Chen, C. Huang, L. Hu, X. Song, Experimental study on mixed-mode fatigue behavior of center cracked steel plates repaired with CFRP materials, Thin Walled Struct. 135 (2019) 486–493.
[10] T. Chen, C. Yao, L. Hu, C. Huang, X. Li, Numerical analysis of central mixed-mode cracking in steel plates repaired with CFRP materials, Thin Walled Struct. 143 (2019) 106196.
[11] L.C. Hollaway, A review of the present and future utilisation of FRP composites in the civil infrastructure with reference to their important in-service properties, Constr. Build. Mater. 24 (12) (2010) 2419–2445.
[12] T. Yu, D. Fernando, J.G. Teng, X.L. Zhao, Experimental study on CFRP-to-steel bonded interfaces, Compos. Part B: Eng. 43 (5) (2012) 2279–2289.
[13] A. Hosseini, E. Ghafoori, M. Wellauer, A.S. Marzaleh, M. Motavalli, Short-term bond behavior and debonding capacity of prestressed CFRP composites to steel substrate, Eng. Struct. 176 (2018) 935–947.
[14] Y. Doroudi, D. Fernando, V.T. Nguyen, J.P. Torres, Experimental study on CFRP-to-steel bonded interfaces under quasi-static cyclic loading, J. Compos. Constr. 23 (4) (2019) 13.
[15] Y. Doroudi, D. Fernando, H. Zhou, V.T. Nguyen, E. Ghafoori, Fatigue behavior of FRP-to-steel bonded interface: An experimental study with a damage plasticity model, Int. J. Fatigue 139 (2020) 17.
[16] H. Zhou, D. Fernando, J.L. Torero, J.P. Torres, C. Maluk, R. Emberley, Bond behavior of CFRP-to-steel bonded joints at mild temperatures: experimental study, J. Compos. Constr. 24 (6) (2020).
[17] H. Zhou, J.P. Torres, D. Fernando, A. Law, R. Emberley, The bond behaviour of CFRP-to-steel bonded joints with varying bond properties at elevated temperatures, Eng. Struct. 183 (2019) 1121–1133.
[18] M. Dawood, S. Rizkalla, Environmental durability of a CFRP system for strengthening steel structures, Constr. Build. Mater. 24 (9) (2010) 1682–1689.
[19] Y. Bai, T.C. Nguyen, X.L. Zhao, R. Al-Mahaidi, Environment-assisted degradation of the bond between steel and carbon-fiber-reinforced polymer, J. Mater. Civ. Eng. 26 (9) (2014) 04014054.
[20] M. Tavakkolizadeh, H. Saadatmanesh, Galvanic corrosion of carbon and steel in aggressive environments, J. Compos. Constr. 5 (3) (2001) 200–210.
[21] L. Arronche, K. Gordon, D. Ryu, V. La Saponara, L. Cheng, Investigation of galvanic corrosion between AISI 1018 carbon steel and CFRPs modified with multi-walled carbon nanotubes, J. Mater. Sci. 48 (3) (2013) 1315–1323.
[22] C. Wu, Y.-Z. Yu, L.-h. Tam, J. Orr, L. He, Effect of glass fiber sheet in adhesive on the bond and galvanic corrosion behaviours of CFRP-Steel bonded system, Compos. Struct. 259 (2021) 113218.
[23] E. Ghafoori, M. Motavalli, J. Botsis, A. Herwig, M. Galli, Fatigue strengthening of damaged metallic beams using prestressed unbonded and bonded CFRP plates, Int. J. Fatigue 44 (2012) 303–315.
[24] E. Ghafoori, M. Motavalli, A. Nussbaumer, A. Herwig, G.S. Prinz, M. Fontana, Determination of minimum CFRP pre-stress levels for fatigue crack prevention in retrofitted metallic beams, Eng. Struct. 84 (2015) 29–41.
[25] A. Hosseini, E. Ghafoori, M. Motavalli, A. Nussbaumer, X.-L. Zhao, Mode I fatigue crack arrest in tensile steel members using prestressed CFRP plates, Compos. Struct. 178 (2017) 119–134.
[26] A. Hosseini, A. Nussbaumer, M. Motavalli, X.-L. Zhao, E. Ghafoori, Mixed mode I/II fatigue crack arrest in steel members using prestressed CFRP reinforcement, Int. J. Fatigue 127 (2019) 345–361.
[27] L. Li, T. Chen, N. Zhang, Y. Hidekuma, Test on fatigue repair of central inclined cracked steel plates using different adhesives and CFRP, prestressed and non-prestressed, Compos. Struct. 216 (2019) 350–359.
[28] H. Heydarinouri, A. Nussbaumer, M. Motavalli, E. Ghafoori, Multiaxial fatigue criteria for prestressed strengthening of steel connections, Int. J. Fatigue 153 (2021).
[29] S.M. Hosseini, J. Melchior, M. Izadi, E. Ghafoori, Fatigue crack arrest in steel beams using FRP composites, Eng. Fail. Anal. 127 (2021).
[30] M. El-Tahan, M. Dawood, G. Song, Development of a self-stressing NiTiNb shape memory alloy (SMA)/fiber reinforced polymer (FRP) patch, Smart Mater. Struct. 24 (6) (2015).
[31] B. Zheng, M. Dawood, Fatigue strengthening of metallic structures with a thermally activated shape memory alloy fiber-reinforced polymer patch, J. Compos. Constr. 21 (4) (2017).
[32] B.-T. Zheng, M. El-Tahan, M. Dawood, Shape memory alloy-carbon fiber reinforced polymer system for strengthening fatigue-sensitive metallic structures, Eng. Struct. 171 (2018) 190–201.
[33] A.I. Abdy, M.J. Hashemi, R. Al-Mahaidi, Fatigue life improvement of steel structures using self-prestressing CFRP/SMA hybrid composite patches, Eng. Struct. 174 (2018) 358–372.
[34] L.Z. Li, T. Chen, X.L. Gu, E. Ghafoori, Heat activated SMA-CFRP composites for fatigue strengthening of cracked steel plates, J. Compos. Constr. 24 (6) (2020).
[35] J. Deng, Z. Fei, Z. Wu, J. Li, W. Huang, Integrating SMA and CFRP for fatigue strengthening of edge-cracked steel plates, J. Constr. Steel Res. 206 (2023) 107931.
[36] L. Janke, C. Czaderski, M. Motavalli, J. Ruth, Applications of shape memory alloys in civil engineering structures—overview, limits and new ideas, Mater. Struct. 38 (5) (2005) 578–592.
[37] A. Cladera, B. Weber, C. Leinenbach, C. Czaderski, M. Shahverdi, M. Motavalli, Iron-based shape memory alloys for civil engineering structures: an overview, Constr. Build. Mater. 63 (2014) 281–293.
[38] M.R. Izadi, E. Ghafoori, M. Motavalli, S. Maalek, Iron-based shape memory alloy for the fatigue strengthening of cracked steel plates: effects of re-activations and loading frequencies, Eng. Struct. 176 (2018) 953–967.
[39] M. Izadi, M. Motavalli, E. Ghafoori, Iron-based shape memory alloy (Fe-SMA) for fatigue strengthening of cracked steel bridge connections, Constr. Build. Mater. 227 (2019) 17.
[40] W. Wang, L. Li, A. Hosseini, E. Ghafoori, Novel fatigue strengthening solution for metallic structures using adhesively bonded Fe-SMA strips: a proof of concept study, Int. J. Fatigue 148 (2021) 106237.

[41] W. Wang, W. Zhou, Ye Ma, M. Motavalli, E. Ghafoori, Complete fatigue crack arrest in metallic structures using bonded prestressed iron-based shape memory alloy repairs, Int. J. Fatigue 180 (2024) 108104.
[42] L. Li, S. Wang, T. Chen, E. Chatzi, H. Heydarinouri, E. Ghafoori, Fatigue strengthening of cracked steel plates with bonded Fe-SMA strips, ce/Pap 6 (3-4) (2023) 380–384.
[43] X. Qiang, Y. Wu, Y. Wang, X. Jiang, Novel crack repair method of steel bridge diaphragm employing Fe-SMA, Eng. Struct. 292 (2023) 116548.
[44] Z. Lyu, X. Jiang, X. Qiang, Z. Xu, J. Wang, On-site Fe-SMA strengthening of floorbeam cutout cracks in steel bridge deck, Eng. Struct. 316 (2024) 118607.
[45] N.D. Fernando, Bond Behaviour and Debonding Failures in CFRP-Strengthened Steel Members, Department of Civil and Structural Engineering, The Hong Kong Polytechnic University, Hong Kong, 2010.
[46] L. Li, Bond behavior and debonding failure in Fe-SMA strengthened steel members, ETH Zurich, Zurich, Switzerland, 2023.
[47] M. Shahverdi, J. Michels, C. Czaderski, M. Motavalli, Iron-based shape memory alloy strips for strengthening RC members: material behavior and characterization, Constr. Build. Mater. 173 (2018) 586–599.
[48] X.-L. Gu, Z.-Y. Chen, Q.-Q. Yu, E. Ghafoori, Stress recovery behavior of an Fe-Mn-Si shape memory alloy, Eng. Struct. 243 (2021) 112710.
[49] Z. Dong, Z. Liu, J. Ji, H. Zhu, G. Wu, C. Sun, Characterization of self-prestressing iron-based shape memory alloy bars for new structures, Constr. Build. Mater. 371 (2023) 130795.
[50] E. Ghafoori, E. Hosseini, C. Leinenbach, J. Michels, M. Motavalli, Fatigue behavior of a Fe-Mn-Si shape memory alloy used for prestressed strengthening, Mater. Des. 133 (2017) 349–362.
[51] E. Hosseini, E. Ghafoori, C. Leinenbach, M. Motavalli, S.R. Holdsworth, Stress recovery and cyclic behaviour of an Fe-Mn-Si shape memory alloy after multiple thermal activation, Smart Mater. Struct. 27 (2) (2018) 10.
[52] D.I.H. Rosa, A. Hartloper, A. de Castro e Sousa, D.G. Lignos, M. Motavalli, E. Ghafoori, Experimental behavior of iron-based shape memory alloys under cyclic loading histories, Constr. Build. Mater. 272 (2021) 121712.
[53] E. Ghafoori, M. Neuenschwander, M. Shahverdi, C. Czaderski, M. Fontana, Elevated temperature behavior of an iron-based shape memory alloy used for prestressed strengthening of civil structures, Constr. Build. Mater. 211 (2019) 437–452.
[54] W.J. Lee, R. Partovi-Nia, T. Suter, C. Leinenbach, Electrochemical characterization and corrosion behavior of an Fe-Mn-Si shape memory alloy in simulated concrete pore solutions, Mater. Corros. 67 (8) (2016) 839–846.
[55] S. Wang, L. Li, Q. Su, X. Jiang, E. Ghafoori, Strengthening of steel beams with adhesively bonded memory-steel strips, Thin Walled Struct. 189 (2023) 110901.
[56] re-fer AG. memory-steel prestressing techniques for strengthening and new construction under static and dynamic loading, ⟨https://www.re-fer.eu/wp2022/wp-content/uploads/memory-steel-Vorspannverfahren_EN.pdf⟩.
[57] S&P C-sheet 240 technical data sheet (CSheet240.TDS.EU-EN.V2), S&P Clever Reinforcement Company AG. Seewen, Switzerland.
[58] SikaPower-1277 Product data sheet, Sika Services AG. Zurich, Switzerland, 2018.
[59] Additional product information: Chemical and mechanical properties according to DIN 6701-3:2015-12 for SikaPower-1277., Sika Services AG. Zurich, Switzerland, 2018.
[60] Additional product information: Material properties of SikaPower-1277, Sika Services AG. Zurich, Switzerland, 2018.
[61] S&P Resin 55 HP technical data sheet (Resin55HP.TDS.EU-EN.V3), S&P Clever Reinforcement Company AG. Seewen, Switzerland.
[62] L. Li, W. Wang, E. Chatzi, E. Ghafoori, Experimental investigation on debonding behavior of Fe-SMA-to-steel joints, Constr. Build. Mater. 364 (2023) 129857.
[63] L. Li, E. Chatzi, C. Czaderski, E. Ghafoori, Influence of activation temperature and prestress on behavior of Fe-SMA bonded joints, Constr. Build. Mater. 409 (2023) 134070.
[64] ASTM International. ASTM E647−22b. Standard Test Method for Measurement of Fatigue Crack Growth Rates, PA, United States, 2022.
[65] N. Pichler, W. Wang, J.A. Poulis, E. Ghafoori, Surface preparations and durability of iron-based shape memory alloy adhesively-bonded joints, Int. J. Adhes. Adhes. (2023) 103439.
[66] M. Izadi, A. Hosseini, J. Michels, M. Motavalli, E. Ghafoori, Thermally activated iron-based shape memory alloy for strengthening metallic girders, Thin Walled Struct. 141 (2019) 389–401.
[67] S. Wang, Q. Su, X. Jiang, J. Michels, E. Ghafoori, Fully bonded iron-based shape memory alloy for retrofitting large-scale bridge girders: thermal and mechanical behavior, Structures 65 (2024) 106710.
[68] Data sheet of HBM strain gauges, ⟨https://www.hbm.com/fileadmin/mediapool/hbmdoc/technical/S01265.pdf⟩.
[69] Dassault Systèmes. Abaqus 2016 Analysis User's Guide - Volume II: Analysis, 2016.
[70] Dassault Systèmes. Abaqus 2016 Analysis User's Guide - Volume IV: Elements, 2016.
[71] C.C. Chamis, Simplified composite micromechanics equations for hygral, thermal and mechanical properties, Ann. Conf. of the Society of the Plastics Industry (SPI) Reinforced Plastics/Composites Inst., 1983.
[72] L. Li, S. Wang, E. Chatzi, M. Motavalli, E. Ghafoori, Analysis and design recommendations for structures strengthened by prestressed bonded Fe-SMA, Eng. Struct. 303 (2024) 117513.